

# Hydrodynamics and Mass Transport in Wall Tube and Microjet Electrodes. Simulation and Experiment for Micrometer-Scale Electrodes

James L. Melville,<sup>†</sup> Barry A. Coles,<sup>†</sup> Richard G. Compton,<sup>\*,†</sup> Nafeesa Simjee,<sup>‡</sup> Julie V. Macpherson,<sup>‡</sup> and Patrick R. Unwin<sup>\*,‡</sup>

Physical and Theoretical Chemistry Laboratory, Oxford University, Oxford OX1 3QZ, United Kingdom, and Department of Chemistry, University of Warwick, Coventry CV4 7AL, United Kingdom

Received: June 6, 2002; In Final Form: September 25, 2002

Mass transport to micrometer-sized electrodes in a microjet (wall-tube) electrode configuration is examined experimentally and through finite element modeling. Electrochemical imaging experiments reveal that local mass transport is highly sensitive to the lateral position of the nozzle with respect to the electrode. When these two components are arranged coaxially, there is a pronounced minimum in the mass transfer rate to the electrode, as determined from transport-limited current measurements. Small lateral displacements of the nozzle from the coaxial position lead first to an increase in mass transport, with the current reaching a maximum at a displacement of around one nozzle radius (50  $\mu\text{m}$ ). For larger lateral displacements of the nozzle from the coaxial position, the limiting current gradually decreases with increasing distance. The implications of these observations for practical applications of the microjet electrode are considered. Voltammetric measurements on the oxidation of  $\text{IrCl}_6^{3-}$  in aqueous solution, with the electrode and nozzle coaxial are shown to be in good agreement with simulation of mass transport. Increasing the solution viscosity dramatically decreases mass transport to the electrode, with the reduction in the diffusion coefficient of the redox species as the major factor.

## Introduction

The microjet electrode (MJE)<sup>1</sup> is a miniaturized version of the wall-tube electrode<sup>2–4</sup> in which of a high velocity jet of electrolyte solution, containing an electroactive analyte, impinges from a nozzle onto the surface of an ultramicroelectrode (UME). In previous applications, the MJE system has mainly employed disc-shaped electrodes of 25  $\mu\text{m}$  diameter and a nozzle diameter between 25 and 100  $\mu\text{m}$ .<sup>5,6</sup> In this configuration the MJE has proven attractive for investigating electron-transfer kinetics<sup>5</sup> and coupled solution reactions<sup>6</sup> and for flow analysis.<sup>7</sup> In the latter case, trace-level detection has been facilitated by coupling the MJE with hydrodynamic modulation voltammetry.<sup>7</sup> Many of these studies utilized a naive empirical treatment of mass transport to the wall tube electrode,<sup>2</sup> but we have recently developed a comprehensive model for mass transport in the MJE configuration,<sup>8</sup> which is more generally applicable.

To fully explore the characteristics and capabilities of the MJE, we now consider mass transport with much smaller electrode sizes (5  $\mu\text{m}$  diameter disk UMEs). The reasons for this development are 2-fold. First, it is well established that in quiescent solution, transport to UMEs increases with decreasing electrode size<sup>9</sup> and it is thus interesting to examine the effect of fast convective flow on mass transfer rates under such conditions. Second, we have previously shown that imaging experiments can reveal detailed insights on local mass transfer from an impinging jet,<sup>2</sup> and we should be able to obtain higher resolution images by carrying out such measurements with smaller electrodes. The studies herein focus on understanding

and characterizing local mass transfer in the impinging jet through both imaging experiments and voltammetric measurements carried out with two different redox species,  $\text{IrCl}_6^{3-/2-}$  and  $\text{Fe}(\text{CN})_6^{4-/3-}$ , at a range of solution viscosities. To complement the experimental measurements, simulations have been developed using a finite element fluid dynamics modeling package. The computational approach provides confirmation of the experimental observations and is able to highlight important features of mass transport in the MJE system that are difficult to obtain experimentally, particularly independent investigations of the effect of viscosity and diffusion coefficient on the transport-limited current response.

## Experimental Section

**Chemicals.** All solutions were prepared using Milli-Q reagent water (Millipore Corp., resistivity 18 MQ cm). Solutions of potassium hexachloroiridate(III) ( $1 \times 10^{-3} \text{ mol dm}^{-3}$ , Sigma Aldrich), contained potassium nitrate ( $0.1 \text{ mol dm}^{-3}$ , purity 99.99%, Sigma Aldrich) as a supporting electrolyte. To explore the effect of solution viscosity on the transport-limited current characteristics of the MJE, potassium hexacyanoferrate(II) solutions ( $1 \times 10^{-2} \text{ mol dm}^{-3}$ , Sigma Aldrich) were used, with  $0.5 \text{ mol dm}^{-3}$  of potassium nitrate as a supporting electrolyte, to which different concentrations of sucrose (114.7–239.8 g  $\text{dm}^{-3}$ , Sigma Aldrich) were added. Intrinsic viscosities were determined by using a simple Ostwald viscometer.

**Instrumentation.** The main features of the MJE system were as previously described.<sup>1</sup> The system comprised a Pt disk UME (diameter 5  $\mu\text{m}$ ), fixed in position below a tapered glass nozzle (i.d. 100/ $\mu\text{m}$ ; o.d. 120  $\mu\text{m}$ ). The nozzle was produced by drawing a borosilicate glass capillary (1.16 mm i.d., 2.0 mm o.d., Harvard Apparatus, Kent, U.K.) to a fine point using a

\* Corresponding authors. E-mail: richard.compton@chemistry.oxford.ac.uk, p.r.unwin@warwick.ac.uk.

<sup>†</sup> Oxford University.

<sup>‡</sup> Warwick University.

vertical micropipet puller (Narishige PB7, Tokyo, Japan). The tip of the nozzle was polished flat to the required diameter, on a home-built polishing wheel, fabricated from a PC hard disk drive, using a series of diamond impregnated pads (Buehler, Coventry, U.K.). Flow of the electrolyte solution was delivered at a series of volume flow rates, using a precision dual drive syringe pump (model no. U-74900-15, Cole-Palmer Instrument Company).

The custom built experimental cell comprised a fully detachable Teflon base, which was attached to a cylindrical glass body (diameter 10.4 cm). The total volume of the cell was approximately 380 cm<sup>3</sup>. A zoom video microscope with a CCD camera attachment (on screen resolution of 2.2  $\mu\text{m}$  per pixel) was used to aid the alignment of the nozzle above the UME. The UME was positioned through a small hole (2 mm) in the base of the cell, so that it protruded approximately 1.5 cm, above the bottom of the cell but was submerged below the level of the solution. The cell could be drained, as required, by simply removing excess solution using a syringe.

The UME was a Pt disk electrode, which was prepared as described elsewhere.<sup>10</sup> The ratio of the electrode diameter to that of the surrounding insulator was 1:220, so that the electrode could be considered to sit in an infinite insulating plane. The dimensions of the electrode were measured directly ( $\pm 1 \mu\text{m}$ ) using an Olympus BH2 optical microscope (equipped with Normarski differential interference contrast objectives, range  $\times 50$  to  $\times 1000$  magnification).

For mass transfer imaging measurements, a home-built SECM<sup>11</sup> was used to scan the nozzle at a constant height, over the surface of the fixed electrode. The nozzle was supported in a home-built capillary holder attached to a piezoelectric positioner (model no. P-843.30, Physik Instrumente, Waldbronn, Germany) which was used to control movement of the nozzle in the  $z$ -direction (normal to the UME) over a maximum expansion of 45  $\mu\text{m}$ . The piezoelectric positioner was, in turn, mounted on a translational stage (M-015.00, Physik Instrumente), controlled by a differential micrometer (model DM-13). This facilitated a larger range of movement in the  $z$ -axis (25 mm) with micrometer resolution. Movement of the  $x$  and  $y$  stages, to which the nozzle was also connected, was achieved using DC-mike drives (M223.21 Physik Instrumente), controlled via a signal processor (C-852, Physik Instrumente) and 2-axis DC motor controller cards (C-842.20, Physik Instrumente). The positions of each axis were determined by digital encoders (MT25, Heidenhain, Germany) with a resolution of 0.1  $\mu\text{m}$ . The entire experimental assembly was placed on a Newport CSD series breadboard within a home-built Faraday cage. This apparatus was, in turn, located on a home-built vibration isolation table.

All voltammetric measurements were made in a two-electrode arrangement, with a silver wire serving as a quasi-reference electrode (AgQRE) and the Pt disk UME as the working electrode. Electrochemical measurements were made using a voltage scan generator (Colburn Electronics, Coventry), and a home-built current follower (gains of  $10^{-5}$  to  $10^{-9}$  A/V). Data were recorded directly to a PC using a Lab-PC-1200 data acquisition card (National Instruments, Austin, TX).

## Experimental Procedures

Experiments were conducted by initially aligning the nozzle, with the solution containing the redox species flowing over the electrode, so that the current for the transport-controlled electrolysis of the analyte of interest was at its maximum value. As discussed below, this corresponded to a position where the

**TABLE 1: Parameters That Define the Geometry of the MJE Cell Used in the Numerical Simulations**

radius of inlet tube, $r_T$	50 $\mu\text{m}$
electrode radius, $r_{\text{elec}}$	2.5 $\mu\text{m}$
electrode-inlet height, $H$	500 $\mu\text{m}$
centerline-outlet length, $l$	600 $\mu\text{m}$

nozzle was in the vicinity of the UME. This task was greatly aided by the use of video microscopy to observe the position of the nozzle relative to the UME. Electrochemical images were then acquired over a region of approximately 400  $\mu\text{m}$  square, with a series of unidirectional scans, usually with a step size of 5  $\mu\text{m}$  between lines, with data acquired every 2  $\mu\text{m}$  on a line. With a scan speed of 10  $\mu\text{m s}^{-1}$ , it typically took 90 min to acquire a complete image. For all imaging experiments, the UME was held at a potential sufficient to oxidize the analyte of interest ( $\text{Fe}(\text{CN})_6^{4-}$ ,  $\text{IrCl}_6^{3-}$ ) at a mass-transport controlled rate.

To ensure that the nozzle was at the same separation from the electrode for each experiment, the nozzle was gently contacted on the surface of the electrode and then retracted from it a specified distance (500  $\mu\text{m}$ ) using the micrometer controlled  $z$ -stage. Distances were measured on screen using a zoom video microscope. All measurements were made in an air-conditioned laboratory ( $23 \pm 0.5^\circ\text{C}$ ).

## Computational Approach

Numerical simulations were carried out with the finite element fluid dynamics package, FIDAP<sup>TM</sup> (version 8.52) (Fluent Europe Ltd., Sheffield, UK, <http://www.fluent.com>), executed on a Silicon Graphics Origin 2000. The convergence values used by FIDAP's internal solution software for each degree of freedom at each node was set to  $10^{-7}$  for the flow solution and  $10^{-5}$  for the diffusion solution. Simulation required 3.5–6.5 min of CPU time for the flow solution and 8–10 min for the diffusion calculation.

The general approach adopted to carry out simulations of the MJE is given in detail in a previous paper<sup>8</sup> and the reader is directed to that reference for more information. However, some improvements to the approach were made and these are discussed below.

**Flow Simulation.** The geometry of the 2-D axially symmetric model used to determine the radial and axial velocities,  $u_r$  and  $u_z$ , is defined by the parameters given in Table 1. An outline of the mesh used in the simulations has the form given by Figure 1, with mesh faces marked, with the number of nodes and type of meshing in each face defined in Table 2. There are two ways of meshing using FIDAP, map meshing, and pave meshing. Map meshing requires that the opposing edges of each mesh face contain the same number of nodes, and this produces a mesh of rectangular quadrilateral elements across that mesh face. Pave meshing removes the requirement for an equal number of nodes on opposing edges and therefore can be used to generate fewer elements across an area of simulation, reducing CPU time. Paved meshing results in elements of a less regular quadrilateral shape.

The arrangement and placing of mesh faces are fundamentally similar to those used to simulate the flow in previous work,<sup>8</sup> with some important modifications. Formerly, the area that contains the elements between the nozzle exit and the mapped area above the electrode surface consisted of a single paved mesh face. Map meshing was found to give a quicker solution, and therefore the amount of paved elements was minimized in this area by splitting the old face into three parts. A small paved mesh face was situated adjacent to the mapped mesh face above the electrode surface, and similarly, another was placed adjacent

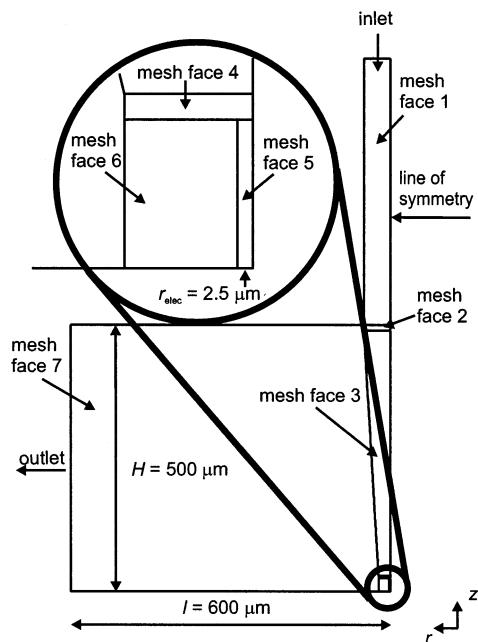


**Figure 1.** Outline of the 2-D axially symmetric model and mesh faces, specified in Table 2, used to simulate the flow to the MJE. The mesh faces are marked, but to aid clarity, the elements are not shown. The expanded area shows the area near the electrode surface, where particularly dense meshing is necessary.

to the map meshed nozzle exit. A large map meshed face linked the two paved faces. Boundary conditions were applied in exactly the same way as previously discussed.<sup>8</sup> These are given in Table 3.

**Diffusion Simulation.** It is undesirable to simulate the concentration over the entire volume of the MJE cell. First, the deviation in bulk concentration at nodes outside the diffusion layer is negligible and extending the simulation into this zone does not contribute to the accuracy of the solution and wastes CPU time. Second, there will be far more nodes situated outside the diffusion layer than are situated near the electrode, and this could cause the internal convergence check of FIDAP to report that there has been little average change to the variable being solved between consecutive iterations, causing the solver to reach the convergence limit too soon, giving rise to an inaccurate-limiting current.

Both of these problems were solved by carrying out the diffusion simulation on a separate mesh, the limits of which are no more than a few microns away from the electrode in both the  $r$  and  $z$  directions, the exact value dependent on the flow rate, viscosity, and diffusion coefficient that is employed in the simulation. FI-CONV, a module of FIDAP, allows the interpolation of the flow calculated in the first part of the simulation onto a new mesh more suitable for the diffusion calculation. With the interpolated flow values, the diffusion calculation can be carried out with all the nodes in the simulation placed relatively near the electrode surface. The diffusion submodel mesh is shown in Figure 2 and is generated by the values in Table 2.

The submodel is a rectangular area consisting of two rectangular mesh faces of equal length in the  $z$ -direction, one beside the other (as drawn in Figure 2). The lower mesh face contains the electrode surface and the area above it, and the upper rectangle contains the area of the surface of the wall adjacent to the electrode. The limits of the submodel area are defined by  $z_{\max}$  and  $r_{\max}$ , the furthest distance simulated in the axial and radial directions, respectively.

**TABLE 2: Mesh Edge Parameters Used To Generate the Mesh Faces That Constitute the Flow Model Shown in Figure 1 and Diffusion Submodel Shown in Figure 2**

mesh face	start coordinate, <sup>a</sup> $p_1$	end coordinate, <sup>a</sup> $p_2$	no. of nodes, $N$	spacing ratio, $q$	type of meshing	no. of elements in mesh face
Flow Model						
1	$(H, 0)$	$(H + 500, 0)$	50	3	mapped	500
	$(H, r_T)$	$(H + 500, r_T)$	50	3		
	$(H, 0)$	$(H, r_T)$	10	3		
	$(H + 500, 0)$	$(H + 500, r_T)$	10	3		
2	$(H - 10, 0)$	$(H, 0)$	6	1	paved	2256
	$(H, 0)$	$(H, r_T)$	10	3		
	$(H - 10, r_T)$	$(H, r_T)$	31	1		
	$(H - 10, 0)$	$(H - 10, r_T)$	7	1		
3	$(30, 0)$	$(H - 10, 0)$	80	1	mapped	2480
	$(30, 22.5)$	$(H - 10, r_T)$	80	3		
	$(30, 0)$	$(30, 22.5)$	31	1		
	$(H - 10, 0)$	$(H - 10, r_T)$	31	1		
4	$(25, 0)$	$(30, 0)$	10	1	paved	97
	$(25, 22.5)$	$(30, 22.5)$	8	1		
	$(25, 0)$	$(25, r_{\text{elec}})$	51	1		
	$(25, r_{\text{elec}})$	$(25, 22.5)$	40	40		
5	$(30, 0)$	$(30, 22.5)$	31	1	mapped	3570
	$(0, 0)$	$(25, 0)$	70	50		
	$(0, r_{\text{elec}})$	$(25, r_{\text{elec}})$	70	50		
	$(0, 0)$	$(0, r_{\text{elec}})$	51	1		
6	$(25, 0)$	$(25, r_{\text{elec}})$	51	1	mapped	2800
	$(0, r_{\text{elec}})$	$(25, r_{\text{elec}})$	70	50		
	$(0, 22.5)$	$(25, 22.5)$	70	1		
	$(0, r_{\text{elec}})$	$(0, 22.5)$	40	40		
7	$(25, r_{\text{elec}})$	$(25, 22.5)$	40	40	paved	750
	$(0, 22.5)$	$(25, 22.5)$	70	1		
	$(25, 22.5)$	$(30, 22.5)$	8	1		
	$(30, 22.5)$	$(H - 10, r_T)$	80	3		
	$(H - 10, r_T)$	$(H, r_T)$	31	1		
	$(0, 22.5)$	$(0, l)$	35	50		
	$(H, r_T)$	$(H, l)$	30	40		
Diffusion Submodel						
1	$(0, 0)$	$(z_{\text{max}}, 0)$	225	3.4	mapped	16875
	$(0, r_{\text{elec}})$	$(z_{\text{max}}, r_{\text{elec}})$	225	3.4		
	$(0, 0)$	$(0, r_{\text{elec}})$	51	7		
	$(z_{\text{max}}, 0)$	$(z_{\text{max}}, r_{\text{elec}})$	51	7		
2	$(0, r_{\text{elec}})$	$(z_{\text{max}}, r_{\text{elec}})$	225	3.4	mapped	11475
	$(0, r_{\text{max}})$	$(z_{\text{max}}, r_{\text{max}})$	225	3.4		
	$(0, r_{\text{elec}})$	$(0, r_{\text{max}})$	75	60		
	$(z_{\text{max}}, r_{\text{elec}})$	$(z_{\text{max}}, r_{\text{max}})$	75	60		

<sup>a</sup> The coordinates are in units of micrometer.

The exact value of the maximum axial distance simulated,  $z_{\max}$ , is dependent on the flow rate, viscosity, diffusion coefficient, and electrode geometry. Initially, an attempt was made to calculate  $z_{\max}$  by using Albery and Bruckenstein's analogy between the wall tube electrode and the rotating disk electrode (RDE).<sup>4</sup> The rotation speed of the RDE,  $\omega$ , in  $\text{rad s}^{-1}$ , is replaced with  $\omega'$ :

$$\omega' = V_f / r_T^3 \quad (1)$$

where  $V_f$  is the volume flow rate and  $r_T$  is the radius of the inlet tube. Then, the diffusion layer,  $\delta$ , can be found by<sup>12</sup>

$$\delta = 1.6118 \nu^{1/6} D^{1/3} \omega'^{-1/2} \quad (2)$$

where  $\nu$  is the kinematic viscosity and  $D$  is the diffusion coefficient. However, it was found that the predicted diffusion layer thickness using this equation for the lowest flow rate and highest viscosity investigated ( $V_f = 0.001667 \text{ cm}^3 \text{ s}^{-1}$ ,  $\nu = 0.01778 \text{ cm}^2 \text{ s}^{-1}$ ,  $D = 3.00 \times 10^{-6} \text{ cm}^2 \text{ s}^{-1}$ ,  $r_T = 50 \times 10^{-4} \text{ cm}$ ) for a cell with a geometry specified by Table 1 gave a predicted diffusion layer of  $1.03 \mu\text{m}$ , far smaller than the value



**TABLE 3: Summary of Boundary Conditions Used To Calculate the Flow Profile and Solve the Diffusion in the MJE Simulation**

Flow Model			
parabolic flow at inlet	$0 \leq r \leq 50$ $r = r_T$	$z = H + 500$ $H \leq z \leq H + 500$	$u_z = (2V_T/\pi r_T^4) r^2$ ; $u_r = 0$
walls	$r_T \leq r \leq l$ $r_{\text{elec}} \leq r \leq l$	$z = H$ $z = 0$	$u_z = 0$ ; $u_r = 0$
electrode	$0 \leq r \leq r_{\text{elec}}$	$z = 0$	$u_z = 0$ ; $u_r = 0$
centerline	$r = 0$	$0 \leq z \leq H + 500$	$u_r = 0$
Diffusion Submodel			
bulk concentration at $z_{\text{max}}$	$0 \leq r \leq r_{\text{max}}$	$z = z_{\text{max}}$	$C_{r,z} = C_{\text{bulk}}$
no concentration at electrode surface	$0 \leq r \leq r_{\text{elec}}$	$z = 0$	$C_{r,z} = 0$

actually obtained by the numerical simulation, 22  $\mu\text{m}$ . It should be noted that the Albery and Bruckenstein approach does not take into account electrode size, which may explain the large discrepancy. The limitations of their approach were highlighted in part 1 of this series of papers.<sup>8</sup>

A general technique can be applied at all conditions to set  $z_{\text{max}}$  successfully, consisting of two steps. First, a value of  $z_{\text{max}}$  was chosen that would be large enough to contain the entire change in concentration from the electrode surface where the concentration is zero to a distance where several nodes have a value of bulk concentration,  $C_{\text{bulk}}$ .

Having found the distance over which all the concentration change occurs, the area of the simulation can then be reduced to include only the diffusion layer. By inspection of the concentration at the nodes along the line of symmetry, a distance was chosen where the concentration was lower than the bulk by 0.01%. This was set as  $z_{\text{max}}$  and the boundary condition of concentration at  $z_{\text{max}}$  set to 99.99% of the bulk for all  $r$ . When the number of nodes placed in the area where concentration change is occurring is maximized, the simulation is re-run to get the highest accuracy possible. The time necessary for the initial diffusion calculation (8–10 min of CPU time) was considered small enough that this was a justifiable approach.

The radial boundary of the submodel,  $r_{\text{max}}$ , was set at 20  $\mu\text{m}$ .

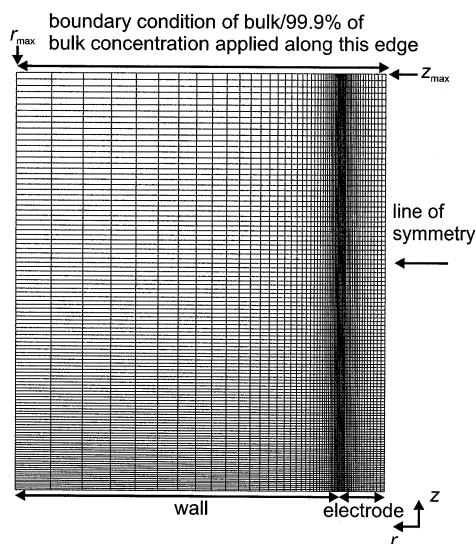


**Figure 2.** Example of the axially symmetric 2-D submodel used to calculate the transport to the electrode, consisting of a rectangular area near the electrode surface. It extends radially 20  $\mu\text{m}$  away from the center of the electrode. The axial distance from the surface of the electrode over which the simulation is carried out is set at the point where the concentration at the centerline reaches 99.99% of bulk. The elements grow smaller at the electrode edge to reduce errors occurring due to the singularity at the boundary edge between electrode and wall. The mesh faces are defined in Table 2.

Simulating beyond this point radially was found to contribute less than 0.01% to the total flux at all viscosities and flow rates simulated.

Analogous to the node placement in the flow model, the node density was made to vary along certain edges of the mesh faces, to place more nodes close to areas of large changes in concentration. This can be seen in Figure 2. In the  $z$ -direction, the node density increases slightly as the electrode surface is approached. In the  $r$ -direction, the node density increases toward the edge of the electrode, to reduce the error that arises from the singularity occurring at the boundary change from electrode to inert surface.<sup>13,14</sup>

Apart from the bulk concentration boundary condition applied at  $z = z_{\text{max}}$ , the only other boundary condition specified is that of zero concentration at the electrode surface. The flux boundary conditions are summarized in Table 3.

## Results and Discussion

**Imaging Experiments.** Mass transfer imaging experiments involved recording the transport-limited current, for the one-electron oxidation of the analyte of interest, as a function of jet position. The nozzle was positioned at a constant height (500  $\mu\text{m}$ ) above the Pt UME (diameter 5  $\mu\text{m}$ ), and then scanned in a series of unidirectional lines over the electrode surface. Initial experiments were conducted using  $\text{IrCl}_6^{3-}$  (1 mM), with a background electrolyte as outlined earlier.

A typical mass transfer-limited current image recorded at the UME, at a volume flow rate of 1.0  $\text{cm}^3 \text{min}^{-1}$ , as a function of nozzle position is shown in Figure 3. In this image, the currents have been normalized with respect to the transport-limited current recorded in quiescent solution ( $i_d = 0.74 \text{ nA}$ ). This figure clearly illustrates the significant enhancements in current that can be achieved using the MJE arrangement, with a relatively low volume flow rate. The steady-state convective-diffusion limiting current can be almost an order of magnitude larger than the current in quiescent solution, but the value is very sensitive to the location of the nozzle with respect to the electrode. In particular, it can be seen that in the center of the image, where the UME and nozzle are aligned, the current actually tends to a pronounced minimum. Moving away from this position radially, it is clear that this minimum is surrounded by a ring of enhanced current, which then decreases with further displacement of the nozzle in the radial direction.

The appearance of a current minimum in the center of the image where the UME and nozzle were coaxial was observed at all of the flow rates investigated (0.1–2.0  $\text{cm}^3 \text{min}^{-1}$ ) and with a different mediator,  $\text{Fe}(\text{CN})_6^{4-}$  oxidation. The detailed form of the dependence of current on radial position will be examined further in a future paper.<sup>15</sup> The simplest treatment of mass transport is when the nozzle and electrode are coaxial. With this in mind, the experimental data in Figure 3 have

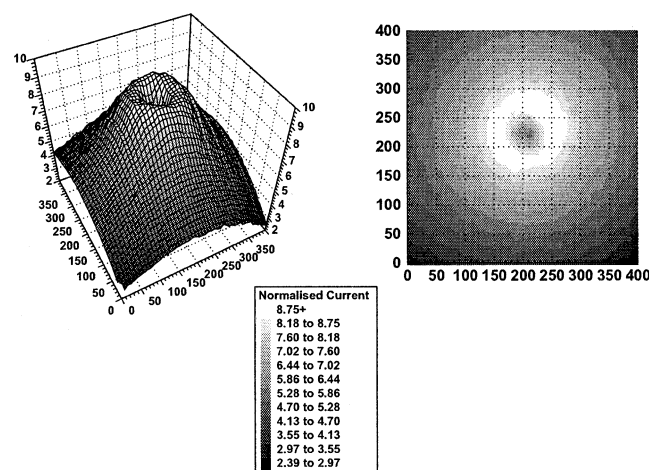


**Figure 3.** Variation of the mass transport-limited current for the oxidation of  $\text{IrCl}_6^{3-}$  (1 mM) at a  $5\ \mu\text{m}$  diameter Pt UME as a function of nozzle position in the  $x$ - $y$  plane, with a volume flow rate of  $1\ \text{cm}^3\ \text{min}^{-1}$ . The nozzle was held at a constant height of  $500\ \mu\text{m}$  above the electrode and scanned over  $400\ \mu\text{m}$  in both the  $x$  and  $y$  directions (plane parallel to the electrode surface). The units for the  $x$  and  $y$  axes in this image is  $\mu\text{m}$ . Currents have been normalized with respect to the limiting current recorded in quiescent solution ( $0.74\ \text{nA}$ ).

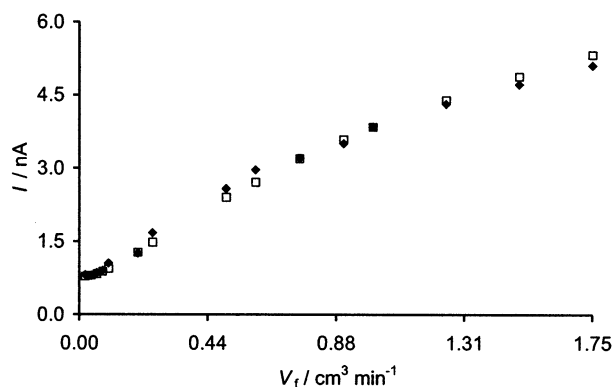


**Figure 4.** Comparison of experimental ( $\blacklozenge$ ) and finite element simulation ( $\square$ ) limiting currents for the oxidation of a 1 mM solution of  $\text{IrCl}_6^{3-}$  at a range of flow rates at a  $5\ \mu\text{m}$  diameter UME. Data used to generate the simulated points are given in Tables 1 and 4.

important implications for the precision with which the nozzle and electrode have to be aligned. In particular, it can be seen that there is only a small tolerance for achieving the current minimum in the coaxial position. Only a slight misalignment of the nozzle and UME leads to the current attaining much greater values. Increasing further the off-set of the nozzle and UME gives a decrease in the transport-limited current, which is a consequence of the solution velocity decreasing as solution moves radially across the surface of the electrode and mixes with the bulk solution.

**Voltammetric Measurements.** The filled diamonds in Figure 4 represent experimental transport-limited currents measured using a MJE cell with a geometry specified in Table 1 for the oxidation of a 1 mM aqueous solution of  $\text{IrCl}_6^{3-}$  containing a supporting electrolyte of potassium nitrate (0.1 M). The squares in Figure 4 are the results of the simulation, using the properties of the solution as specified in Table 4. As can be seen, there is excellent agreement between the experimental and simulated results. On the other hand, in some experiments, transport-limited currents were sometimes larger than expected, which is consistent with the slight misalignment of the nozzle and UME, as already discussed. In terms of the future application of the MJE for voltammetric studies, there would be advantages to

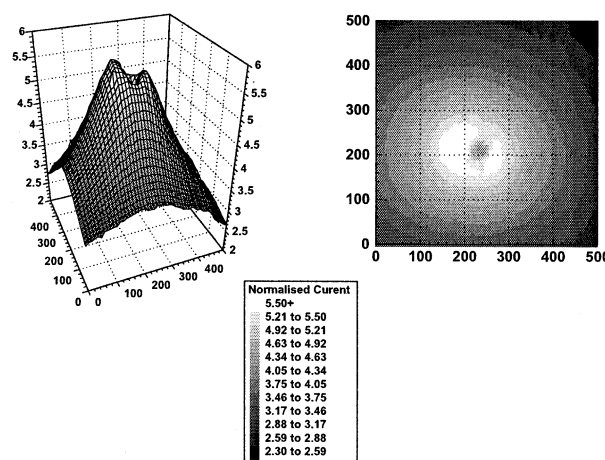


**Figure 5.** Mass transfer image recorded at a  $5\ \mu\text{m}$  diameter Pt UME, for a solution of  $10\ \text{mM}\ \text{Fe}(\text{CN})_6^{4-}$  with the addition of sucrose to achieve a viscosity of  $0.0193\ \text{g}\ \text{cm}^{-1}\ \text{s}^{-1}$ . The image is over an area of  $500 \times 500\ \mu\text{m}$ , which is the scale on the  $x$  and  $y$  axes.

**TABLE 4: Physical Parameters Used To Generate the Simulated Limiting Currents in Figures 4 and 7–10**

curve	$\mu/\text{g}\ \text{cm}^{-1}\ \text{s}^{-1}$	$D/\text{cm}^2\ \text{s}^{-1}$	$\rho/\text{g}\ \text{cm}^{-3}$	$c_{\text{bulk}}/\text{mol}\ \text{cm}^{-3}$
Figure 4				
( $\square$ )	0.00888	$8.01 \times 10^{-6}$	0.998	$1.0 \times 10^{-6}$
Figure 7				
a ( $\blacklozenge$ )	0.010	$6.00 \times 10^{-6}$	1.044	$1.0 \times 10^{-5}$
b ( $\blacksquare$ )	0.014	$4.29 \times 10^{-6}$	1.091	$1.0 \times 10^{-5}$
c ( $\blacktriangle$ )	0.017	$3.53 \times 10^{-6}$	1.110	$1.0 \times 10^{-5}$
d ( $\times$ )	0.020	$3.00 \times 10^{-6}$	1.125	$1.0 \times 10^{-5}$
Figure 8				
a ( $\bullet$ )	0.010	$6.00 \times 10^{-6}$	1.044	$1.0 \times 10^{-5}$
b ( $\circ$ )	0.010	$6.00 \times 10^{-6}$	1.125	
Figure 9				
a ( $\blacklozenge$ )	0.010		$6.00 \times 10^{-6}$	
b ( $\blacksquare$ )	0.014	$6.00 \times 10^{-6}$	1.091	$1.0 \times 10^{-5}$
c ( $\blacktriangle$ )	0.017	$6.00 \times 10^{-6}$	1.110	$1.0 \times 10^{-5}$
d ( $\times$ )	0.020	$6.00 \times 10^{-6}$	1.125	$1.0 \times 10^{-5}$
Figure 10				
a ( $\blacklozenge$ )	0.010	$6.00 \times 10^{-6}$	1.044	
b ( $\blacksquare$ )	0.010	$4.29 \times 10^{-6}$	1.091	$1.0 \times 10^{-5}$
c ( $\blacktriangle$ )	0.010	$3.53 \times 10^{-6}$	1.110	$1.0 \times 10^{-5}$
d ( $\times$ )	0.010	$3.00 \times 10^{-6}$	1.125	$1.0 \times 10^{-5}$

working in the position of maximum current. This would be easier to achieve practically, as well as delivering higher mass transfer rates, enabling the study of fast kinetics. However, mass transport in this configuration is necessarily three-dimensional and more complicated to treat computationally.

**Effect of Viscosity.** The next stage of the investigations involved varying the solution viscosity, through the addition of sucrose to a solution of  $0.01\ \text{mol}\ \text{dm}^{-3}\ \text{Fe}(\text{CN})_6^{4-}$  ( $0.5\ \text{mol}\ \text{dm}^{-3}\ \text{KNO}_3$  supporting electrolyte). The effect of solution viscosity on mass transfer to the MJE has not previously been examined, but such studies should provide useful information on the most important factors controlling the limiting current. Four different viscosities were investigated:  $0.0093$ ,  $0.0127$ ,  $0.0149$ , and  $0.0193\ \text{g}\ \text{cm}^{-1}\ \text{s}^{-1}$ , with solutions prepared and characterized as described earlier. Complete images of transport-limited current, as a function of nozzle position, were recorded at each viscosity at a flow rate of  $1\ \text{cm}^3\ \text{min}^{-1}$ . Voltammograms were then obtained at different volume flow rates with the nozzle and electrode closely co-aligned.

A typical mass transfer image for  $\text{Fe}(\text{CN})_6^{4-}$  oxidation with a solution viscosity of  $0.0193\ \text{g}\ \text{cm}^{-1}\ \text{s}^{-1}$  is shown in Figure 5. It is noticeable that the transport-limited current enhancements

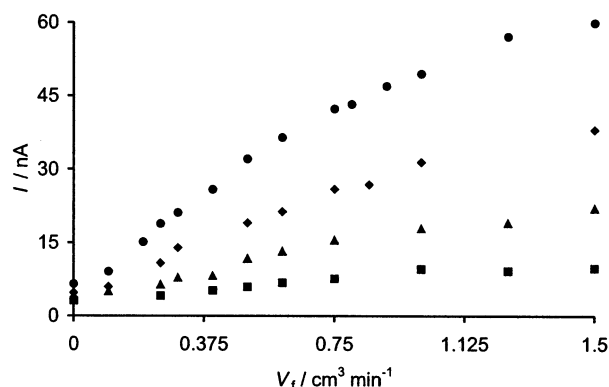


**Figure 6.** Summary of voltammetric limiting current data for  $\text{Fe}(\text{CN})_6^{4-}$  (10 mM) oxidation for several viscosities: (●)  $0.0093 \text{ g cm}^{-1} \text{ s}^{-1}$ , (◆)  $0.0127 \text{ g cm}^{-1} \text{ s}^{-1}$ , (▲)  $0.0149 \text{ g cm}^{-1} \text{ s}^{-1}$ , and (■)  $0.0193 \text{ g cm}^{-1} \text{ s}^{-1}$ . For these experiments the nozzle was positioned within ca.  $10 \mu\text{m}$  of the coaxial arrangement. Measured physical data are given in Table 5.

**TABLE 5: Measured Physical Parameters Corresponding to the Data in Figure 6 (at  $23^\circ\text{C}$ )**

sucrose concn/ $\text{g dm}^{-3}$	$\rho/\text{g cm}^{-3}$	$\mu/\text{g cm}^{-1} \text{ s}^{-1}$	$D/10^{-6} \text{ cm}^2 \text{ s}^{-1}$
0	1.00	0.0093	6.74
114.7	1.08	0.0127	4.87
170.2	1.10	0.0149	4.30
239.8	1.12	0.0193	3.21

are less than measured in sucrose-free solutions, but the overall form of the image is similar to that already discussed for lower viscosity solutions (Figure 3). The reasons for the diminution in current are explored through simulations reported below.

Further experiments involved steady-state current–voltage measurements to investigate the effect of viscosity on transport-limited currents. Typical results at a series of solution viscosities are shown in Figure 6, from which it can clearly be seen that there is a significant effect of solution viscosity on mass transport under both quiescent and convective-diffusion conditions. The viscosities and diffusion coefficients relevant to Figure 6, derived from viscometry and steady-state limiting current measurements are given in Table 5, along with the measured solution densities.

Although there is a lack of perfect alignment (up to ca.  $10 \mu\text{m}$ ) of the nozzle and electrode in the experiments used to generate the data in Figure 6, the importance of the viscosity is clear. A series of theoretical simulations were therefore carried out to investigate the effects of viscosity on the current–flow rate response. In these, different values of viscosity and diffusion coefficient were chosen to obey Walden's rule: the product of viscosity and conductivity is approximately a constant for the same ions in different solvents.<sup>16</sup> Hence the product of viscosity and diffusion coefficient should also be a constant. Values of viscosity and diffusion coefficient were chosen so that

$$\mu D = 6.00 \times 10^{-8} \text{ g cm s}^{-2} \quad (3)$$

where  $\mu$  is the dynamic viscosity (in  $\text{g cm}^{-1} \text{ s}^{-1}$ ) and  $D$  is the diffusion coefficient (in  $\text{cm}^2 \text{ s}^{-1}$ ). This resulted in a dynamic viscosity of  $0.010 \text{ g cm}^{-1} \text{ s}^{-1}$  when the diffusion coefficient was  $6.00 \times 10^{-6} \text{ cm}^2 \text{ s}^{-1}$ . It can be seen from Table 5 that this is fairly typical of the values for an aqueous solution containing  $\text{Fe}(\text{CN})_6^{4-/3-}$  under the experimental conditions. The precise values used for all the simulations detailed below are compiled in Table 4.

For each viscosity, a series of limiting currents at the MJE was simulated for a 10 mM solution of  $\text{Fe}(\text{CN})_6^{4-/3-}$  at 10

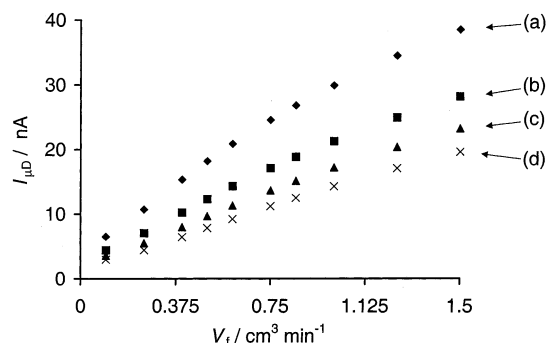


**Figure 7.** Simulated limiting current against volume flow rate at the MJE with a Pt electrode of radius  $2.5 \mu\text{m}$  for a solution of 10 mM  $\text{Fe}(\text{CN})_6^{4-/3-}$ , with four different viscosities each with their own value of  $D$ . The curves were generated with the values given in Table 4.

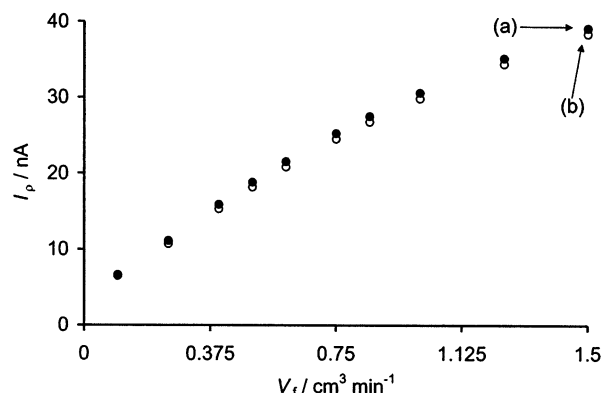


**Figure 8.** Simulated limiting against volume flow rate at the MJE with a Pt electrode of radius  $2.5 \mu\text{m}$  for a solution of 10 mM  $\text{Fe}(\text{CN})_6^{4-/3-}$ , illustrating the effect of changing density with fixed values of viscosity and diffusion coefficient. The curves were generated with the values given in Table 4.

different flow rates, between  $0.1$  and  $1.5 \text{ cm}^3 \text{ min}^{-1}$ . The results are shown in Figure 7. As would be expected, an increase in viscosity and the commensurate decrease in diffusion coefficient reduces the current at all flow rates. It is also clear that there is qualitative agreement between the computational results and experimental observations.

When examining the effect of viscosity on limiting current, it is revealing to elucidate which has the largest effect: the increased viscosity or decreased diffusion coefficient? Though experimentally it would be extremely difficult, if not impossible, to produce a series of solutions at different viscosities but with identical diffusion coefficients (or vice versa), the computational approach lends itself extremely well to answering such questions.

Though it was anticipated that the main effect on current reflected the viscosity and diffusion coefficient, there is also a change of density with viscosity to consider. To quantify any change to the current caused by a change in density, a new series of flow rates were simulated, with the same physical properties as in curve a in Figure 7, but with a higher density,  $1.125 \text{ g cm}^{-3}$ . This density corresponds to that which would be found at a viscosity of  $0.020 \text{ g cm}^{-1} \text{ s}^{-1}$ , according to experiment. The results are shown in Figure 8. It can be seen that there is very little effect on the limiting current, the difference being less than 4% at all flow rates. Therefore it can be concluded that the effect on current is due overwhelmingly to changes in diffusion coefficient and viscosity.

To quantify the relative contributions of diffusion coefficient and viscosity to the change in current, another series of

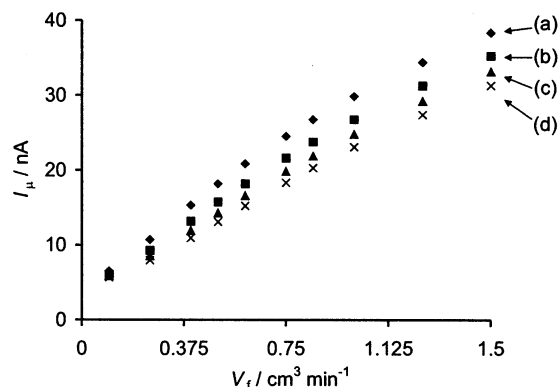


**Figure 9.** Simulated limiting against volume flow rate at the MJE with a Pt electrode of radius  $2.5 \mu\text{m}$  for a solution of  $10 \text{ mM Fe(CN)}_6^{4-/3-}$ , illustrating the effect of viscosity with fixed values of diffusion coefficient. The curves were generated with the values given in Table 4.

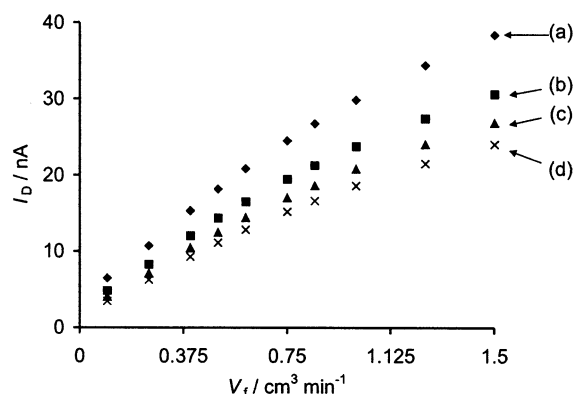


**Figure 10.** Simulated limiting against volume flow rate at the MJE with a Pt electrode of radius  $2.5 \mu\text{m}$  for a solution of  $10 \text{ mM Fe(CN)}_6^{4-/3-}$ , illustrating the effect of diffusion coefficient with fixed values of viscosity. The curves were generated with the values given in Table 4.

simulations were carried out. The first used the same flow rate range and viscosities (and their respective density values) that were used to produce Figure 8, but with the diffusion coefficient fixed at  $6.00 \times 10^{-6} \text{ cm}^2 \text{ s}^{-1}$ , thus showing the effect on limiting current of changing the viscosity (the effect of changing density having been shown to be negligible). The results shown in Figure 9. The second set of simulations were carried out with the same diffusion coefficients used to generate Figure 7, but with the viscosity and density values held constant (at  $0.010 \text{ g cm}^{-1} \text{ s}^{-1}$  and  $1.044 \text{ g cm}^{-3}$ , respectively). These results are shown in Figure 10.

From Figure 9 it can be seen that there is only a small difference between the limiting currents as viscosity is altered. The effect of doubling viscosity causes a drop in simulated limiting current from curve a to curve d of between 13 and 29%, whereas the drop is 49–59% in Figure 7, when both viscosity is doubled and the diffusion coefficient is halved. This suggests that the reduction in  $D$  is mainly responsible for the change in limiting current, as confirmed by the curves in Figure 10, where the diffusion coefficient is halved, but the viscosity is held constant. Here, the drop in current from curve a to curve d ranges between 37 and 47%.

To quantify the degree to which the diffusion coefficient and viscosity are responsible for the drop in current, we define three parameters:  $\Delta I_{\mu D}$ ,  $\Delta I_{\mu}$ , and  $\Delta I_D$ .  $\Delta I_{\mu D}$  is defined as

$$\Delta I_{\mu D} = I_{\mu D(a)} - I_{\mu D(x)} \quad (4)$$

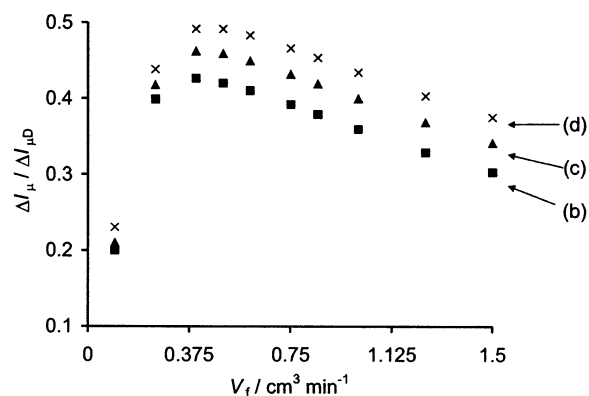


**Figure 11.** Graph to show the relative importance of viscosity on the limiting current at different flow rates and values of  $\mu$ , produced by comparison of Figures 7 and 9. The higher the value of  $\Delta I_{\mu} / \Delta I_{\mu D}$ , the more important the effect of changing viscosity on the flow rate, relative to diffusion coefficient.

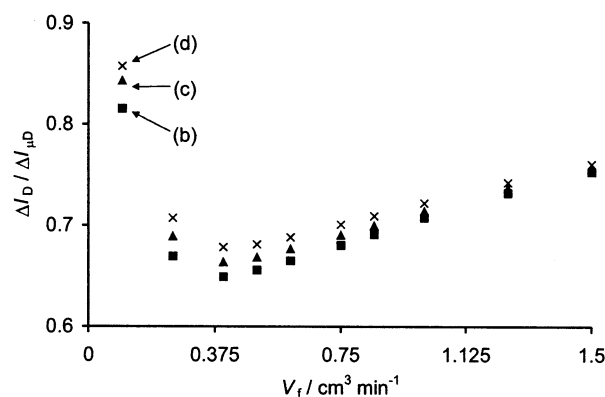


**Figure 12.** Graph to show the relative importance of diffusion coefficient on the limiting current at different flow rates and values of  $D$ , produced by comparison of Figures 7 and 10. The higher the value of  $\Delta I_D / \Delta I_{\mu D}$ , the more important the effect of changing diffusion coefficient on the flow rate, relative to viscosity.

where  $I_{\mu D(a)}$  is the limiting currents obtained for curve a in Figure 7 and  $I_{\mu D(x)}$  is the limiting currents obtained for curve x, where “x” can be either b, c, or d. An analogous procedure generates  $\Delta I_{\mu}$ , and  $\Delta I_D$ , but using Figures 9 and 10, respectively:

$$\Delta I_{\mu} = I_{\mu(a)} - I_{\mu(x)} \quad (5)$$

$$\Delta I_D = I_{D(a)} - I_{D(x)} \quad (6)$$

A plot of  $\Delta I_{\mu} / \Delta I_{\mu D}$  against  $V_f$  is shown in Figure 11.  $\Delta I_{\mu} / \Delta I_{\mu D}$  can vary between 0, where viscosity has no contribution to the current difference at that flow rate, and 1, where the change in viscosity is entirely responsible for the change in current at that flow rate. As can be seen from Figure 11,  $\Delta I_{\mu} / \Delta I_{\mu D}$  is less than 0.5 for all flow rates and viscosities, showing that, under Stokes–Einstein conditions, the reduction in diffusion coefficient is the most important single factor for the reduced limiting current at higher viscosities. At any given flow rate, increasing the viscosity increases its relative effect on the limiting current, but it never becomes more than the effect of diffusion coefficient. Confirmatory data is given by Figure 12, a plot of  $\Delta I_D / \Delta I_{\mu D}$  against  $V_f$ , with the same range of values applying, but with respect to diffusion coefficient.  $\Delta I_D / \Delta I_{\mu D}$  is always greater than 0.5. In Figures 11 and 12 the flow rate dependence reflects a balance between the change from the microdisk diffusion only limit, as convection is increased, and the effect of viscosity on the flow rate local to the electrode.



From these theoretical simulations it can be concluded that both viscosity and the diffusion coefficient are extremely important in determining the transport-limited current in a MJE at typically encountered experimental conditions, with the diffusion coefficient playing the most important role.

### Conclusions

Modeling and experiment have allowed mass transport to micrometer-sized electrodes in the microjet (wall tube) configuration to be characterized for the first time. With the nozzle and disk-shaped UME coaxial, so that the MJE system is axisymmetric, experimental limiting current measurements for  $\text{IrCl}_6^{3-}$  oxidation are in good agreement with simulation. Under these conditions, increasing the viscosity of the solution results in a significant decrease in mass transfer rate, mainly through a reduction in the diffusion coefficient of the redox probe molecule, though viscosity has a small intrinsic effect on the limiting current.

Electrochemical imaging experiments highlight the very high precision with which the nozzle and electrode have to be aligned in order that the experimental configuration conforms to the axisymmetric model. As the nozzle is displaced laterally from this position, mass transport to the electrode, from the action of the impinging jet, increases up to a distance of about one nozzle radius displacement. Although more difficult to treat computationally, this configuration could be attractive for practical measurements with the MJE. First, this arrangement would be easier to configure in the position of maximum current. Indeed, it is anticipated that simple manual micrometer-driven stages could be utilized. Second, because the mass transport rate in this position can be almost twice as large as for the

axisymmetric configuration, this arrangement is potentially more sensitive for analytical and kinetic measurements. Future work will consider the quantitative treatment of mass transport under these conditions.

**Acknowledgment.** We thank EPSRC for a studentship for N.S. and J.L.M. J.V.M. thanks the Royal Society for a University Research Fellowship.

### References and Notes

- (1) Macpherson, J. V.; Marcar, S.; Unwin, P. R. *Anal. Chem.* **1994**, 66, 2175.
- (2) Chin, D. T.; Tsang, C. H. *J. Electrochem. Soc.* **1978**, 125, 1461.
- (3) Brett, C. M. A.; Oliveira-Brett, A. M. *Electrochemistry*; Oxford University Press: Oxford, U.K., 1993.
- (4) Albery, W. J.; Bruckenstein, S. *J. Electroanal. Chem.* **1983**, 144, 105.
- (5) Macpherson, J. V.; Beeston, M. A.; Unwin, P. R. *J. Chem. Soc., Faraday Trans.* **1995**, 91, 899.
- (6) Martin, R. D.; Unwin, P. R. *J. Electroanal. Chem.* **1995**, 397, 325.
- (7) Macpherson, J. V.; Unwin, P. R. *Anal. Chem.* **1999**, 71, 4642.
- (8) Melville, J.; Simjee, N.; Unwin, P. R.; Coles, B. A.; Compton, R. G. *J. Phys. Chem. B* **2002**, 106, 2690.
- (9) Forster, R. *J. Chem. Soc. Rev.* **1994**, 23, 289.
- (10) Macpherson, J. V.; Unwin, P. R. *J. Phys. Chem.* **1994**, 98, 1704.
- (11) Evans, N. J. Ph.D. Thesis, University of Warwick, 1999.
- (12) Levich, V. G. *Physicochemical Hydrodynamics*; Prentice Hall: Englewood Cliffs, NJ, 1962.
- (13) Ferrigno, R.; Brevet, P. F.; Girault, H. H. *Electrochim. Acta* **1997**, 42, 1895.
- (14) Galceran, J.; Gavaghan, D. J.; Rollett, J. S. *J. Electroanal. Chem.* **1995**, 394, 17.
- (15) Melville, J.; Simjee, N.; Unwin, P. R.; Coles, B. A.; Compton, R. G. Manuscript to be submitted.
- (16) Meites, L. *Polarographic Techniques*, 2nd ed.; Wiley-Interscience: New York, 1958.